UVP MEASUREMENTS OF THE FLOW BEHIND A ROTATING CIRCULAR CYLINDER

Yoshihiro Inoue*, Akira Ito** and Shintaro Yamashita*

* Dept. Mathematical & Design Eng., Gifu University, 1-1 Yanagido, Gifu 501-1193, Japan
E-mail: inouey@cc.gifu-u.ac.jp, yamasita@cc.gifu-u.ac.jp

** Graduate School of Eng., Gifu University, 1-1 Yanagido, Gifu 501-1193, Japan
E-mail: i3132005@guedu.cc.gifu-u.ac.jp

ABSTRACT

Separated flow past a rotating circular cylinder has been investigated by flow visualizations and velocity profile measurements using the ultrasonic Doppler method. Experiments were performed in a free-surface water channel with Re_d = 800, a Reynolds number larger than the critical Reynolds number of the flow behind a circular cylinder, within a rotational speed ratio range of U_c^* = 0 to 6. Flow visualized images were obtained by the dye method and captured with the digital video camera. Fluctuating velocity fields, v (y, t), measured by the UVP monitor were represented in contour maps and analyzed with the POD. Wake patterns are divided into two main categories in terms of the rotational speed ratio; (i) regular vortex street within the lower speed range and (ii) disordered vortex structure within the higher range. There are three subcategories between two main-categories. It is shown that the fluctuation energy within the wake shear layers, and the deflection amount and width of the shear layer are changed with the rotational speed ratio.

Keywords : Cylinder Wake, Centrifugal Instability, Flow Visualization, Shear Layer Oscillation

INTRODUCTION

It is an important engineering issue in relation to the occurrence of flow-induced vibration and/or airborne noise to illuminate a large-scale structure formed behind a bluff body in a uniform flow [1-3]. When a circular cylinder is rotating around its axis, the wake is accompanied by several characteristic phenomena and more complicated in comparison with a case where the circular cylinder is not rotating. One reason for this difference is that the flow separation phenomenon occurs not from the wall surface of the circular cylinder but from the inside of the fluid [4]. Another reason is that the secondary flow is induced by centrifugal instability [5]. These two phenomena exert a considerable influence on the location of the flow separation and the behavior of the separated shear layer, playing a dominant role in the formation process of the flow structure in the entire wake. One of the effectual parameters is the ratio of the rotational speed of the circular cylinder U_c to the uniform flow velocity U_0, which is denoted as $U_c^* = U_c / U_0$. Flow structures in the wakes are expected to vary with U_c^*.

Glauert [6, 7] analyzed the two-dimensional flow passing by a circular cylinder placed in a uniform flow as to a case where separation phenomenon was not seen at a high rotational speed ratio based on the boundary layer theory. Moore [8] also put a flow field at a high rotational speed ratio to theoretical analysis. Moore approached this issue by utilizing small perturbation from exact solution at the infinite rotational speed ratio. On the other hand, Swanson [9] overviewed the studies in Magnus force acting on a rotational body made by 1960. Koromilas and Telionis [10] examined an unsteady laminar separation through the flow visualization and with a laser Doppler velocimeter. In the numerical study, including the discrete vortex simulation by Ingham [11] and Cheng *et al*. [12], a number of research papers have been presented since the latter half of the 1980s.

This study is designed to experimentally treat the flow behind a circular cylinder rotating uniformly in a uniform stream, and identify the wake vortex structures by varying the rotational speed ratio U_c^* and classify them accordingly. Since the dependency of this flow field on Reynolds number is not negligible, care should be directed to the selection of an experimental Reynolds number. In this study, experiment was conducted with Re_d = 800, a Reynolds number larger than the critical Reynolds number of the flow behind a circular cylinder, within a rotational speed ratio range of U_c^* = 0 to 6. In order to observe and identify the flow patterns, the flow fields were visualized by the dye method, and then the flow velocity pattern visualization was applied by using an ultrasonic velocity profile (UVP) monitor [13]. Furthermore, the feature extraction of the velocity variation pattern was conducted by using the proper orthogonal decomposition, and thereby the variation in the wake vortex structure according to the change of the rotational speed ratio was examined.

EXPERIMENTAL PROCEDURE

Apparatus

The experiment was conducted in a water tunnel with an open channel of 700 mm in width, 500 mm in depth and approx. 2000 mm in length to be used as a measurement part. The test channel was provided with an acrylic resin window on both sides. A uniform flow was driven by an inverter-controlled mixed flow pump and settled by a straightener and screens. On the other hand, the circular cylinder was rotated by an AC motor equipped with reduction gear and a toothed belt, and the rotational speed of the circular cylinder was obtained by counting the number of signals detected by an electromagnetic pickup.

The outline of the flow field and its coordinate system are

shown in Fig. 1. The *z*-axis is coincided with the circular cylinder axis, the *x*-axis is coincided with the uniform flow direction, and the *y*-axis is taken at right angles to both the axes. The circular cylinder is rotated in the direction as shown in the figure. At this time, when $y > 0$, the circular cylinder surface speed is in the direction opposite to the direction of the main stream, and when $y < 0$, the circular cylinder surface speed is in the same direction as the direction of the main stream. The former is called "pressure side" and the latter "suction side" in likening to the air flow around a wing. The diameter of the circular cylinder used in this experiment was $d = 20$ mm, and the reference Reynolds number was $Re_d = U_0\, d\, /\, \nu = 800$ (uniform velocity $U_0 \approx 40$ mm/s). The rotational speed ratio of the circular cylinder $U_c^* = U_c\, /\, U_0 = \omega\,(d\, /\, 2)\, /\, U_0$ was varied within a range of 0 to 6 (rotational angular speed $\omega \approx 0$ - 24 rad/s).

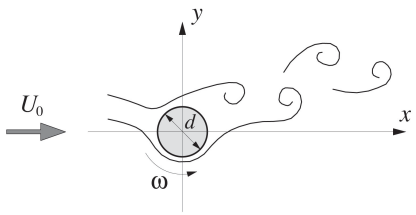

Fig. 1 Flow field and coordinate system.

Flow visualization technique

For the flow visualization, the electrolytic precipitation method and the dye image method using Uranine were utilized. Both the methods are the same in that the circular cylinder surface is used as a dye source, while the latter enables localized visualization by means of sheet light illumination since Uranine is a fluorescent dye. In fact, since the three-dimensional nature of the flow field, *i.e*., variation in the *z*-direction, was not negligible, the laser light sheet technique was utilized in the dye image method to grab images visualized within the *x*-*y* plane. The laser used was Ar-ion laser with an output of 500 mW. On the other hand, the electrolytic precipitation method was utilized to observe the three-dimensional nature of the flow in the span direction, and the *x*-*z* plane was illuminated with a higher-output straight tube type mercury lamp. However, the images captured by this method were omitted in the present paper.

The visualized images were grabbed with a digital video camera (SONY TRV900) and recorded in a mini DV tape. The captured images were transferred from a DV recorder (Panasonic NV-DM1) to a PC, and processed on the PC. In reconstructing the visualized images based on Taylor's hypothesis, a necessary range of pixels were cut out of 600 images with a frame rate of 30 fps, and connected in chronological order to obtain a single image.

UVP measurement method

Ultrasonic velocity profile (UVP) measurement is conducted in such a way that an ultrasonic beam is emitted into the water and the ultrasonic Doppler-echoes from the seeding particles within the water are detected and analyzed. For Met-Flow Model X3-PS used in this experiment, the same ultrasonic transducer is utilized both to send and to receive an ultrasonic wave, and the instantaneous velocity information $\tilde{v}_\xi$ on the ultrasonic beam is measured as the function of the distance ξ in the beam direction. By repeating this procedure temporally, the time-series data of velocity profile $\tilde{v}_\xi(\xi, t)$ is obtained.

In this experiment, an ultrasonic transducer with the basic frequency of 4 MHz and 5 mm in diameter was used. The ultrasonic beam was directed in parallel with the *x*-direction and the *y*-direction, and $\tilde{u}\,(x, t)$ and $\tilde{v}\,(y, t)$ were measured, respectively. At this time, as ultrasonic scattering particles, hydrogen bubbles continuously generated from a platinum wire of 80 μm in diameter located in the upstream of the measurement position were used. When it comes to the space and time sampling intervals under the operating conditions of this experiment, the time interval was about 38 ms, and the space intervals was 2.96 mm in the *x*-direction profile and 2.22 mm in the *y*-direction profile.

In processing the velocity profile data, the space and time profile $\tilde{v}_\xi(\xi, t)$ of the instantaneous velocity component in the ξ-direction is divided into the mean component and the fluctuating component, and expressed as $\tilde{v}_\xi(\xi, t) = V_\xi\,(\xi) + v_\xi\,(\xi, t)$. Then, the fluctuating component profile is analyzed by using Fourier transform and POD to examine the space and time variable characteristics of the flow field. This procedure should be referred to Inoue *et al*. [14].

RESULTS AND DISCUSSION

Flow visualizations by the dye images

The dye pattern emitted from the Uranine coated over the circular cylinder was illuminated with a laser light sheet positioned in parallel with the *x*-*y* plane. The images captured in this method are shown in Fig. 2. The rotational speed ratios of the shown images were $U_c^* = 0$, 1.0, 1.85, 2.0, 3.0, 4.0 and 5.0. As evident from the figure, changes in the wake pattern due to the rotational speed ratio U_c^* are significant. At $U_c^* = 0$, a vortex street subjected to alternative shedding due to the roll-up of the separated shear layer is observed. Also at $U_c^* = 1.0$, the shear layer separated on the pressure side and suction side was rolled up, respectively, composing a vortex street similar to that at $U_c^* = 0$. However, differences from the flow field at $U_c^* = 0$ lie in that the cylindrical vortex formation region is closer to the circular cylinder and that the center axis of the vortex street is deviated upwards from the *x*-axis.

Here, it should be noted in this visualization method that the dye is emitted from the circular cylinder surface but the flow separation points are not existent on the circular cylinder surface except for the case at $U_c^* = 0$. Since the dye supply to the separated shear layer is not so reliable as seen at $U_c^* = 0$, there is no choice but to reply on other dye transport mechanism. That is, the dye is carried out of the surface through the boundary layer adhered to the circular cylinder surface and rotating together, and carried away to the downstream by the flow in the outer layer. In the photo of the case at $U_c^* = 1.0$, the separated shear layer from the pressure side is visualized as a layer with a high dye concentration, while no such layer is seen on the suction side. At $U_c^* = 1.85$ and 2.0, the layer with a high dye concentration is not observed on the pressure side or the suction side, and a very narrow dead water area is seen behind the circular cylinder. There is little dye pattern appeared showing the vortex street in the wake, but only dye streaks have feebly ordered features.

When the rotational speed is faster, the flow in the boundary layer is under a strong centrifugal instability, and a vortex structure similar to Taylor vortex around the circular cylinder [13].

This vortex receives a supply of dye from the circular cylinder surface, forming a banded area with a high dye concentration. This vortex area breaks away from the circular cylinder under the influence of the flow in the outer layer. These behaviors are clearly seen in the photos of $U_c^* = 3.0$ and 4.0. The complicatedly winding dye patterns fill in the broad layer almost disorderly. At a higher rotational speed ratio of $U_c^* = 5.0$, the boundary layer on the circular cylinder appears turbulent, and dye patterns of various scales, like turbulent eddies, can be seen in the wake shear layer.

Contrast with the dye images and velocity contour maps

In this section, the contrast between the dye patterns shown in Fig. 2 and the flow field is considered at a location comparatively near to the circular cylinder, $x / d = 3$. For this purpose, the visualized images are reconstructed based on Taylor's hypothesis and shown in Fig. 3. The flow field is obtained from the y-direction UVP measurement at $x / d = 3$, and shown as a contour map of the fluctuating velocity $v(y, t)$ in Fig. 4. In the figure, the solid line represents the positive fluctuating velocity contour and the broken line the negative fluctuating velocity contour. The results are shown as to the cases with the rotational speed ratios $U_c^* = 0$, 1.0, 1.85, 3.0 and 5.0, respectively.

In contrast of dye patterns between the flow fields with $U_c^* = 0$ and 1.0, there is a difference in dye concentration, there is agreement in the fundamental structure that the cylindrical vortex areas are arranged alternately with the center axis between them and these two areas are connected staggeringly. There is a good agreement in fluctuating velocity contour between these rotational speed ratios, representing the y-direction velocity field induced to the cylindrical vortices of the staggered arrangement. At $U_c^* = 1.85$, there is no dye pattern corresponding to the well-organized cylindrical vortices, but rather the dye pattern like zigzagged lines is dominant. In correspondence with the weakening of the cylindrical vortices, there is no longer the orderliness in the v-fluctuation pattern, and the fluctuation amplitude is considerably weakened in comparison with that at $U_c^* = 0$ and 1.0.

On the other hand, the dye pattern at $U_c^* = 3.0$ forms a widening layer of streaky, high-dye-concentration area originated in Taylor vortex, and its coherence is low. This is also clearly seen in the v-fluctuation contour map. Furthermore, the fluctuation energy within the layer is considerably low. Lastly, in the flow field at $U_c^* = 5.0$, like in the flow field at $U_c^* = 3.0$, the visualized pattern is seen with dye lumps filled in the wide layer. In comparison with these two flow fields, the layer at $U_c^* = 5.0$ is considerably wider, the individual dye lumps are of more complicated shape and of more minute segmentation, and the dye concentration is lower. However, there is an organized velocity fluctuation area seen in the v-fluctuation contour map. This implies the generation of an organized motion whose image is different from that of the flow at $U_c^* \leq 3.0$.

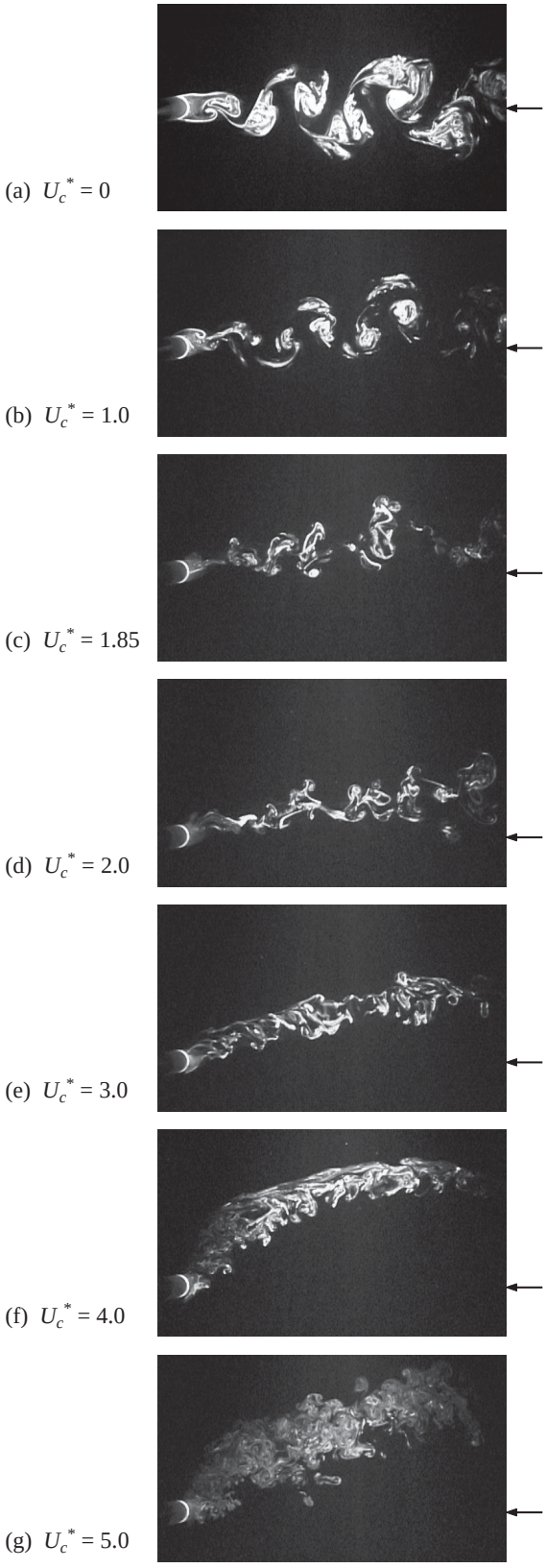

Fig. 2 Plan views of wakes behind the rotating circular cylinder visualized with a thin laser light sheet.

Lateral fluctuating velocity field

In order to quantitatively discuss the variation in the flow structure according to the rotational speed ratio considered until the preceding section, the y-direction UVP measurement data is analyzed statistically. Figure 5 shows the total energy of the v-fluctuation within the wake shear layer, E_v, in relation to the rotational speed ratio. Here, E_v is defined by the following equation:

$$E_v = \frac{1}{T}\int_{-T/2}^{T/2}\int v^2(y,t)\,dy\,dt = \int \overline{v^2}(y)\,dy\,. \qquad (1)$$

It is evident from the figure that the high fluctuation energy held at $U_c^* < 1$ sharply decreases along with the increase in the rotational speed ratio within a range of $1 < U_c^* < 1.7$, and fur-

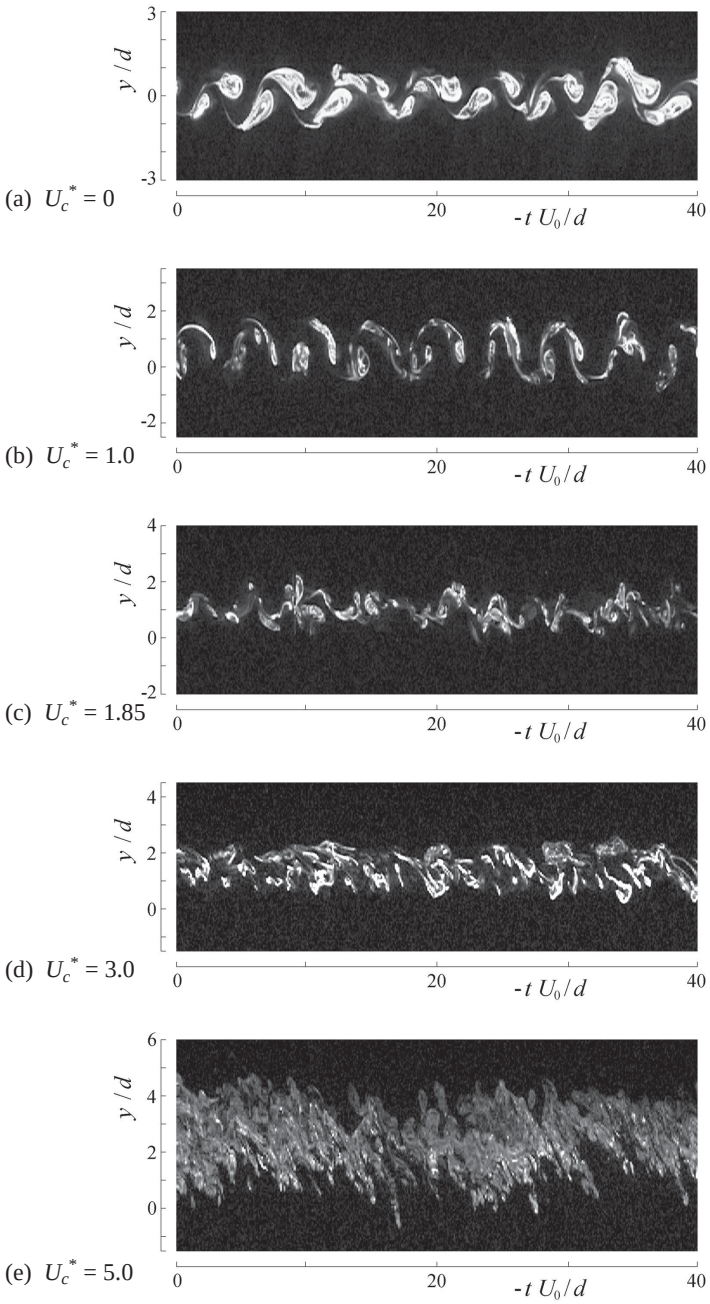

Fig. 3 Dye images based on the Taylor's hypothesis

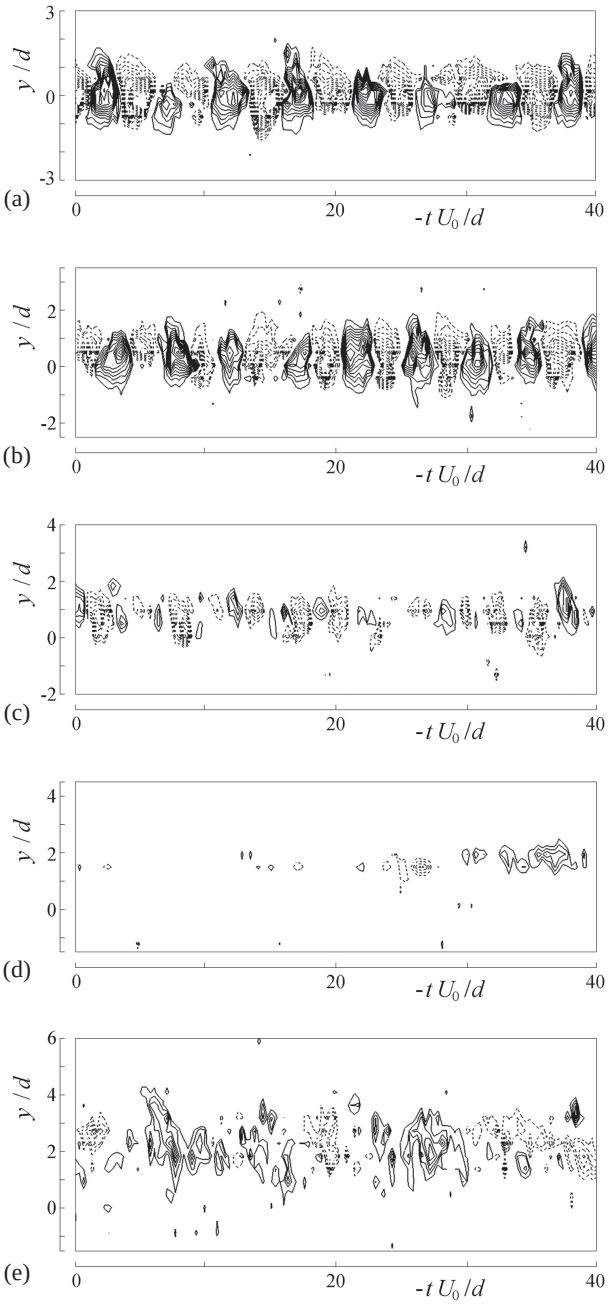

Fig. 4 Contour maps of velocity fluctuation in the *y*-direction.

ther slowly decreases within a range of $1.7 < U_c^* < 3$. E_v remains little changed within a range of $3 \le U_c^* \le 4$, and increases again when $U_c^* \ge 5$.

Next, the lateral-direction fluctuation characteristics of the shear layer are analyzed by the POD method, and the spatial mode of the *v*-fluctuation profile is identified firstly. The eigenvalues, $\lambda_v^{(n)}$ and the empirical eigenvectors, $\phi_v^{(n)}$ are shown in Figs. 6 and 7, respectively. Here, n is an integer representing the mode, and only the results of $n = 1$ and 2 are shown in these figures. The eigenvalues, i.e., the ratio of contribution from each mode to the total energy, are as high as 75 to 80% at $U_c^* \le 1.25$ only in the 1st mode. Then, the contribution ratio sharply decreases along with the increase in the rotational speed ratio within a range of $1.25 < U_c^* < 3.5$ down to the minimum ratio of 25% at $U_c^* = 3.5$. The contribution ratio $\lambda_v^{(1)}$ increases along with the rotational speed ratio within a range of $3.5 < U_c^* < 5$ up to over approx. 40% at $U_c^* \ge 5$. On the other hand, the contribution ratio $\lambda_v^{(2)}$ remains lower than the contribution ratio $\lambda_v^{(1)}$. It takes the maximum value of 12% at $U_c^* = 2.25$, and shows almost constant value within a range of $3 \le U_c^* \le 4$, and reaches approx. 15% at $U_c^* = 5.0$. It is evident from these results that there is a distinguished mode in the *v*-fluctuation profile of the wake in the vicinity of the rotating circular cylinder, and that, except for the rotational speed ratio range of $3 \le U_c^* \le 4$, the spatial fluctuations in the 1st and 2nd modes make the energy contribution of 50 % or more.

In Fig. 7, the eigenvectors of these modes are normalized by using the maximum value of $\phi_v^{(1)}$, and also the *y*-coordinate is normalized by using the position y_c in which the $\phi_v^{(1)}$ is the maximum value and the half-value width $b_{0.5}$ of the $\phi_v^{(1)}$ profile. From this scaling, the eigenvectors have similar distributions at all rotational speed ratios within the experimental range. It is evident from this that the spatial mode with dominant *v*-fluctuation receives almost no influence of the rotational speed

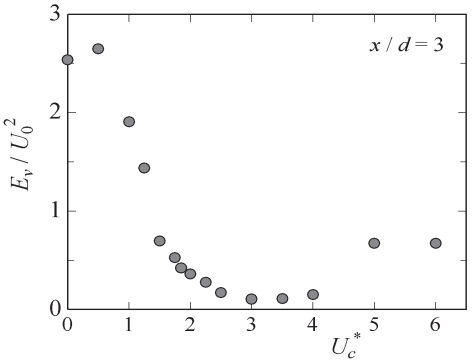

Fig. 5 Energy of *v*-fluctuation at $x / d = 3$.

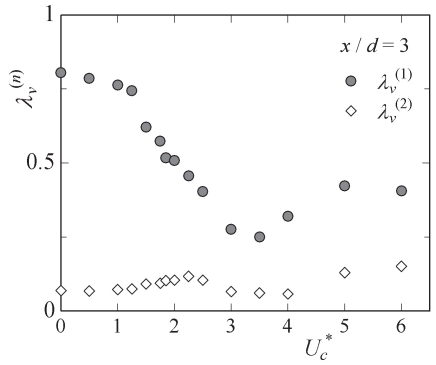

Fig. 6 Eigenvalues in the 1st and 2nd mode.

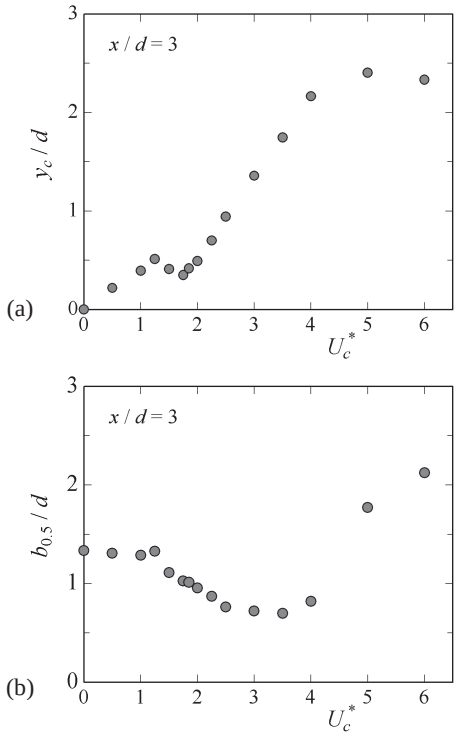

Fig. 8 Center position and width of the shear layer.

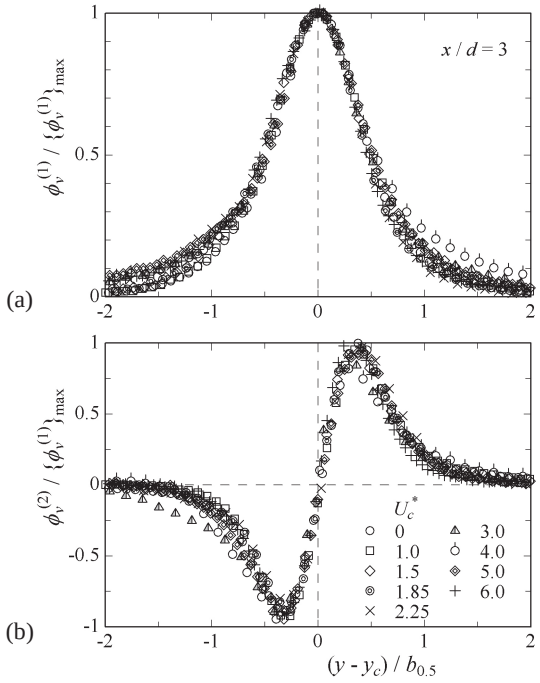

Fig. 7 Distributions of the eigenfunction at the first two POD modes.

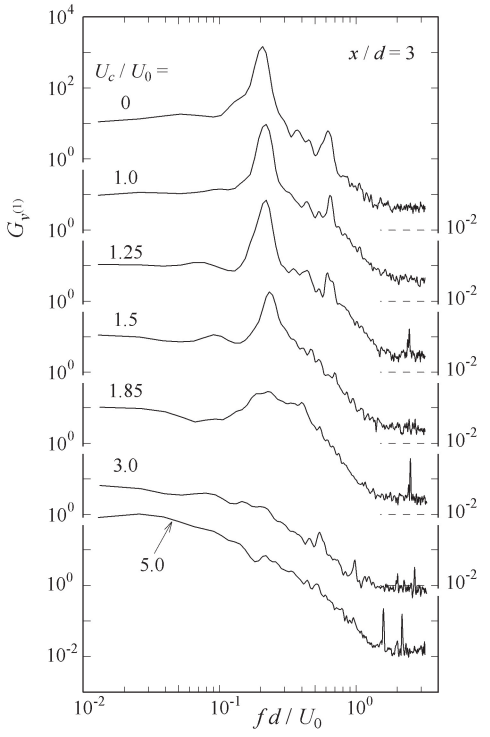

Fig. 9 Power spectrum of the random coefficient of *v*-fluctuation in the first POD mode at $x / d = 3$.

ratio. Furthermore, it is interpreted that the 1st mode representing the bell-shaped distribution shows the *y*-direction fundamental oscillation of the shear layer and that the 2nd mode, which is an odd function, shows the expansion and compression around the center axis of the shear layer.

The relation of y_c and $b_{0.5}$, which characterize the spatial scale of the wake shear layer, to the rotational speed ratio are shown in Fig. 8. The coordinates, y_c can be interpreted as the center of the shear layer, that is, the magnitude of the wake deflection due to the rotation of the circular cylinder can be estimated. On the other hand, $b_{0.5}$ indicates the *y*-direction scale of the shear layer. From Fig. 8(a), it is seen that y_c increases almost linearly at $U_c^* \leq 1.25$. It reaches the relative maximum of 0.51 *d* at $U_c^* = 1.25$, then increases monotonously from the minimum value of 0.35 *d* at $U_c^* = 1.75$ up to 2.4 *d* at $U_c^* = 5.0$, and then almost flattens out at $U_c^* \geq 5$. In contrast, it is seen from Fig. 8(b) that the half-value width $b_{0.5}$ shows almost a constant value of 1.3 *d*, then, in a range of $1.25 < U_c^* < 3$, de-

creases monotonously along with the increase in the rotational speed ratio, then in a range of $3 \le U_c^* \le 4$, shows approx. 0.7 d with little change, then, at $U_c^* > 4$, increases sharply, and then reaches 2.1 d at $U_c^* = 6.0$.

Spectra of the random coefficient

Lastly, the spectrum obtained as a result of Fourier transform of the velocity fluctuation is described. According to the analysis by the POD method of the *v*-fluctuation distributions described in the preceding section, the space mode of the fluctuation is identified, and the information in the time direction is obtained by projecting the fluctuation data set to each spatial mode. This is called "random coefficient" and defined by the following equation:

$$v^{(n)}(t) = \int v(y,t)\, \phi_v^{(n)}(y)\, dy \ . \qquad (2)$$

By obtaining the spectrum of this coefficient, the occurrence state of each spatial mode can be examined in the frequency space. In this flow field, as shown in Fig. 6, since the fluctuation of the 1st mode is distinguished, the power spectrum of this 1st mode alone is shown in Fig. 9. At $U_c^* \le 1.5$, a spectral peak with the dimensionless frequency $f\,d\,/\,U_0 \approx 0.21$ in the center is seen. This peak frequency increases slightly along with the increase in the rotational speed ratio. At $U_c^* = 1.85$, broadband spectrum having high-energy hump is seen in a range of $f\,d\,/\,U_0 = 0.2$ - 0.4. At $U_c^* \ge 3$, the spectrum monotonously lowers the energy density toward the high-frequency zone, showing the profile similar to turbulent spectrum.

CONCLUSIONS

Results in the present study are put together, this flow field is classified, and the boundary values of the rotational speed ratios are shown in approximate numerical values as follows:

(i) $0 \le U_c^* \le 1.25$: The flow structure is that the staggered arrangement of the cylindrical vortex is dominant, and the deflection amount of the center coordinates of the vortex street increases linearly along with the rotational steed ratio.

(ii) $1.25 < U_c^* < 1.85$: The width of the wake shear layer is narrower in comparison with the lower rotational speed ratio, and the deflection amount of the wake center coordinates decreases due to the increase in the rotational speed ratio.

(iii) $1.85 < U_c^* < 3$: The width of the shear layer and the fluctuation energy contained in the shear layer decrease, together with the lowering of the coherence of fluid motions, along with the increase in the rotational speed ratio.

(iv) $3 < U_c^* < 4$: The flow in the shear layer is inactive, and the width of the shear layer and the fluctuation energy also take the minimum value, but only the deflection amount of the flow in the shear layer increases.

(v) $U_c^* \ge 5$: The disordered vortex structure like turbulent eddy is dominant, and the width of the shear layer and the fluctuation energy increase again.

REFERENCES

1. S. Taneda, 1977, Visual study of unsteady separated flows around bodies, *Prog. Aerospace Sci.*, 17, pp. 287-348.
2. C.H.K. Williamson, 1996, Vortex dynamics in the cylinder wake, *Annu. Rev. Fluid Mech.*, 28, pp. 477-539.
3. T. Leweke, C.H.K. Williamson, 1998, Three-dimensional instabilities in wake transition, *Euro. J. Mech. B/Fluids*, 17, pp. 571-586.
4. J.C. Williams, III, 1977, Incompressible boundary-layer separation, *Annu. Rev. Fluid Mech.*, 9, pp. 113-144.
5. P.G. Drazin, W.H. Reid, 1981, "Hydrodynamic Stability," Cambridge University Press.
6. M.B. Glauert, 1957, A boundary layer theorem, with applications to rotating cylinders, *J. Fluid Mech.*, 2, pp. 89-99.
7. M.B. Glauert, 1957, The flow past a rapidly rotating circular cylinder, *Proc. Royal Soc. London*, Ser. A, 230, pp. 108-115.
8. D.W. Moore, 1957, The flow past a rapidly rotating circular cylinder in a uniform stream, *J. Fluid Mech.*, 2, pp. 541-550.
9. W.M. Swanson, 1961, The Magnus effect: a summary of investigations to date, *Trans. ASME J. Basic Eng.*, pp. 461-470.
10. C.A. Koromilas, D.P. Telionis, 1980, Unsteady laminar separation: an experimental study, *J. Fluid Mech.*, 97, pp. 347-384.
11. D.B. Ingham, 1983, Steady flow past a rotating cylinder, *Computers and Fluids*, 11, pp. 351-366.
12. M. Cheng, Y.T. Chew, S.C. Luo, 1994, Discrete vortex simulation of the separated flow around a rotating circular cylinder at high Reynolds number, *Finite Elements in Analysis and Design*, 18, pp. 225-236.
13. Y. Takeda, 1995, Velocity profile measurement by ultrasonic Doppler method, *Exp. Thermal Fluid Sci.*, 10, pp. 444-453.
14. Y. Inoue, S. Yamashita, K. Kondo, 2002, The ultrasonic velocity profile measurement of flow structure in the near field of a square free jet, *Exp. Fluids*, 32, pp. 170-178.